electronic reprint

Journal of
Applied Crystallography
ISSN 0021-8898
Editor: **Gernot Kostorz**

Small-angle energy-dispersive X-ray scattering using a laboratory-based diffractometer with a conventional source

Giuseppe Portale, Alessandro Longo, Lucio D'Ilario, Andrea Martinelli, Ruggero Caminiti and Valerio Rossi Albertini

Journal of
Applied Crystallography
ISSN 0021-8898

Received 2 November 2005
Accepted 8 December 2006

Small-angle energy-dispersive X-ray scattering using a laboratory-based diffractometer with a conventional source

Giuseppe Portale,[a]*‡ Alessandro Longo,[b] Lucio D'Ilario,[a] Andrea Martinelli,[a] Ruggero Caminiti[a] and Valerio Rossi Albertini[c]

[a]Dipartimento di Chimica, Università degli Studi 'La Sapienza', Piazzale A. Moro 5, 00185 Rome, Italy, [b]Istituto per lo Studio dei Materiali Nanostrutturati del CNR, Via Ugo La Malfa 153, 90146 Palermo, Italy, and [c]Istituto di Struttura della Materia del CNR, Area di ricerca di Tor Vergata, Via del fosso del Cavaliere 100, 00133 Rome, Italy. Correspondence e-mail: portale@esrf.fr

The use of polychromatic *Bremsstrahlung* X-rays generated by commercial tubes for energy-dispersive small-angle scattering measurements has not been extensively discussed in the literature, mainly because of some difficulties associated with it. If a suitable experimental setup is chosen and concomitant phenomena are taken into account for correcting the observed X-ray patterns, energy-dispersive small-angle X-ray scattering (SAXS) may become an interesting alternative to conventional measurements based on monochromatic beams. Energy-dispersive SAXS experiments carried out on protein solutions, micelles, semicrystalline polymers and catalytic systems are discussed to illustrate the new opportunities offered by this technique as well as its limitations.

1. Introduction

With the advent of nano-science, small-angle X-ray scattering (SAXS) has become in recent years a powerful tool to study the structure and morphology of many organic and inorganic systems with features typically in the range of 1–100 nm. This technique provides information about size, shape and aggregation state of biological macromolecules or micelles in solution. Solid-state samples like semicrystalline polymers can also be investigated and information about the separation and size of crystalline and amorphous domains can be extracted. Light can also be shed on the structure of heterogeneous catalytic systems and cluster sizes in alloys (Fratzl, 2003). Furthermore, SAXS can be used to carry out time-resolved studies on the kinetics of phase transitions, *i.e.* structural or morphological transformations of many advanced materials. Assuming the presence of only elastic scattering events, the SAXS intensity depends on the momentum transfer $hq/2\pi$, where q is given by

$$q = \frac{4\pi \sin\theta}{\lambda} = \alpha E \sin\theta, \qquad (1)$$

where α is a constant ($\alpha = 2/hc = 1.014\ \text{Å}^{-1}\,\text{keV}^{-1}$; h = Planck's constant, c = speed of light), λ and E are the wavelength and the energy, respectively, of the X-ray radiation used, and θ is one half of the scattering angle. Two ways can therefore be followed to acquire scattered intensity profiles over the q range of interest. The first consists of using a monochromatic beam and performing an angular scan around the sample (angle-dispersive X-ray small-angle scattering, AD-SAXS). The second consists of using polychromatic radiation and measuring the scattering profile by means of an energy-sensitive detector as a function of the energy of the scattered photons while fixing the scattering angle (energy-dispersive small-angle scattering, ED-SAXS). In the latter case, the *Bremsstrahlung* of an X-ray tube can be used as a polychromatic X-ray primary beam (sometimes referred to as 'white' radiation in analogy with visible light). The energy-dispersive technique has some outstanding advantages over the angular-dispersive counterpart, which can be summarized as follows: (i) reduction of the acquisition time; (ii) a steady apparatus during data collection; (iii) simultaneous collection of the diffuse pattern points.

However, there is a drawback, namely a significant decrease of the q resolution. The relative uncertainty on q can be expressed as

$$\frac{\Delta q}{q} = \cot\theta \Delta\theta + \frac{\Delta E}{E}, \qquad (2)$$

where the first term on the right-hand side of equation (2) originates from the angular divergence of the X-ray beam and the second comes from the finite energy resolution of the detector. For this reason, the ED method is particularly suitable when patterns characterized by long-period oscillations or broad peaks are collected as is typically the case for SAXS.

Up to now, several ED-SAXS studies have been carried out using polychromatic synchrotron sources (Bordas *et al.*, 1976;

‡ Now at: Dubble CRG/ESRF, Netherlands Organisation for Scientific Research (NWO), c/o ESRF, BP 220, F-38043 Grenoble Cedex, France.

Bordas & Randall, 1978; Yu *et al.*, 1999), but only one has been reported where a laboratory facility was used (Schultz & Long, 1975). In that work, the discussion of the characteristics and applicability of this technique was rather limited. For this reason we reported, in a preliminary communication, our results on the possibility of using a laboratory energy-dispersive X-ray diffractometer to perform static and time-resolved small-angle experiments on polymeric materials (Portale *et al.*, 2004).

In the present investigation, the possibility is shown of applying successfully the ED mode on several systems classically studied by SAXS. The data treatment steps needed to obtain correct small-angle profiles have been carefully considered. The results are compared with those obtained using a standard small-angle Kratky camera in order to outline the limits and advantages of the ED-SAXS technique in general, and of the apparatus used here in particular.

2. Theory of ED-SAXS and data reduction

In a typical ED-SAXS experiment performed using a laboratory machine (see §3 for details), the intensity recorded by a solid-state detector placed at a distance $\overline{SD}$ from the sample is

$$\begin{aligned} I_{\rm obs}(E, E', \theta) &= \frac{\text{number of photons collected over } \Delta S}{\text{second}} \\ &= \frac{{r_0}^2}{\overline{SD}}\, G[I_0(E)P(E,\theta)A_{\rm coh}(E,\theta)I_{\rm coh}(E,\theta) \\ &\quad + \frac{E'}{E} I_0(E')P(E',\theta)A_{\rm inc}(E,E',\theta)I_{\rm inc}(E',\theta) \\ &\quad + M(E,E',\theta)], \end{aligned} \tag{3}$$

where ΔS is the scattered X-ray beam cross section selected by the detector window, r_0 is the classic Thompson electron radius, G is the so-called geometrical factor (constant when the setup is fixed), $I_0(E)$ is the energy spectrum of the incident polychromatic beam, $M(E, E', \theta)$ is the multiple scattering term, $P(E, \theta)$ is the polarization factor and the terms A and I are the absorption and the scattered intensity of the sample, respectively. The geometric factor G contains all the quantities modifying the total photon flux at the detector position. The analytical form of G as a function of such quantities is rather complicated. Indeed, G depends in a different manner on the horizontal and vertical apertures of the slits. Furthermore, this dependence differs from slit to slit. A detailed discussion can be found in a previous paper of one of the authors (Rossi Albertini & Paci, 2002). At a given angle (namely once the tube-to-sample and sample-to-detector distances as well as the apertures of all slits are set) G reduces to a constant. The subscripts 'coh' and 'inc' stand for single coherent and incoherent (Compton) scattering, while E' and E are the photon energies before and after the collision of the X-ray photons with the sample electrons, respectively. They can be obtained from the classic Compton relation $\lambda - \lambda' = (h/mc)\,(1 - \cos2\theta)$, by replacing λ with its expression in terms of E ($\lambda = hc/E$). $M(E, E', \theta)$ is the multiple scattering term, which summarizes the contribution to the observed intensity from both the coherent and incoherent events deviating the photon directions more than once. Expression (3) can be simplified. At small angles, the incoherent scattering can indeed be neglected. Multiple scattering can be neglected as well if the sample is thin or not particularly transparent to X-rays. Moreover, the degree of polarization P of a wave after scattering, under the assumption of partial polarization of the wave before being deflected, is

$$P(E,\theta) = \frac{1+\cos^2(2\theta)}{2} + \frac{\sin^2(2\theta)}{2}\frac{I_0^{\perp} - I_0^{\parallel}}{I_0^{\perp} + I_0^{\parallel}}, \tag{4}$$

where $I_0^{\perp}$ and $I_0^{\parallel}$ are the primary beam intensities polarized perpendicularly to and along the scattering plane, respectively. Consequently, the total polarization factor P at small angles is approximately 1 since the quantities $\cos^2(2\theta)$ and $\sin^2(2\theta)$ are close to 1 and 0, respectively.

Under small-angle scattering conditions, an important term to be added to equation (3) is the parasitic scattering due to the collimation system. This parasitic intensity is mainly generated by the scattering of the X-rays from the slit edges, but also from air, since the sample thickness is normally between 1 and 2 mm, while the air path length amounts to 360 mm. As a consequence, the equation describing the detected ED-SAXS intensity becomes

$$\begin{aligned} I_{\rm obs}(E,\theta) &= K[I_0(E)A_{\rm coh}(E,\theta)I_{\rm coh}(E,\theta)] \\ &\quad + K'[I_0(E)A_{\rm coh}(E,\theta)\Pi_{\rm s}(E,\theta)] \end{aligned} \tag{5}$$

where K and K' contain G and the term $(r_0/R)^2$; $\Pi_{\rm s}(E, \theta)$ is the parasitic scattering intensity term.

The coherently scattered intensity per unit volume V, $I_{\rm coh}(E, \theta)$, is given in the most general case by the well known expression

$$I_{\rm coh}(\mathbf{q}) = \frac{1}{V}\iiint \tilde{\rho}^2(\mathbf{r}) \exp(-i\mathbf{q}\cdot\mathbf{r})\,{\rm d}V, \tag{6}$$

where $\tilde{\rho}^2(\mathbf{r})$ is the auto-correlation or Patterson function (Patterson, 1934), $\exp(-i\mathbf{q}\cdot\mathbf{r})$ is the phase factor, V is the volume and r is the distance between two generic scattering centres. Two further restrictions are usually introduced to simplify equation (6): the system is statistically isotropic and no long-range order exists in the sample. These two requisites are fulfilled in all the cases considered here. In the case of dilute solutions of identical particles having constant electron density ρ embedded in a medium of electron density ρ_0, the equation has to be modified by introducing the electron density difference term $\Delta\rho = \rho - \rho_0$. For an ensemble of N independent particles in a volume V we obtain therefore

$$I_{\rm coh}(q) = \frac{N}{V} I_1(q) = (\Delta\rho)^2 V_{\rm part}^2 \frac{N}{V}\int_0^D 4\pi r^2 \gamma_0(r)\frac{\sin qr}{qr}\,{\rm d}r, \tag{7}$$

where $I_1(q)$ is the single particle scattered intensity, $V_{\rm part}$ is the volume of one scattering particle and $\gamma_0(r)$ is the normalized correlation function related to the geometry of the particle. In practice, instead of $\gamma_0(r)$, the function $p(r) = r^2\gamma_0(r)$ is often

used, which describes the distribution of distances between the volume elements inside one particle. The pair distance distribution function $p(r)$ can be computed by inverse Fourier transforming $I_{\rm coh}(q)$. For spherical objects of radius R, the integral in equation (7) can be solved analytically leading to the well known particle intensity function

$$I(q) = (\Delta\rho)^2 V_{\rm part}^2 \frac{N}{V}\left[3\frac{\sin(qR) - qR\cos(qR)}{(qR)^3}\right]^2, \qquad (8)$$

where the quantity between square brackets is the so-called Rayleigh function.

For other geometrical bodies, like ellipsoid cylinders and prisms, semi-analytical expressions can be found (Feigin & Svergun, 1987).

For undiluted systems an interference term must be considered. For spherical particles the overall intensity becomes

$$I(q) = (\Delta\rho)^2 \frac{N}{V} V_{\rm part}^2 P(q) S(q), \qquad (9)$$

where $P(q)$ is the form factor and $S(q)$ is the structure factor of the lattice of interacting particles. For a lattice of spheres of identical size, $P(q)$ assumes the Rayleigh expression reported above. Formulae for both $P(q)$ and $S(q)$ have been derived for a large variety of systems of particles of different shapes and different lattice arrangements. As for the general small-angle scattering (SAS) theory, the reader is referred to the works of Guinier & Fournet (1955) and Glatter & Kratky (1982). Some of these general relations will be recalled in the following.

Some corrections applicable to the ED-SAXS technique are required in equation (5) in order to isolate the scattered coherent intensity from the experimental intensity $I_{\rm sam}^{\rm obs}(E,\theta)$ recorded by the detector. In particular, the following steps are needed.

(i) Normalization of the raw intensity to the incident white-beam spectral profile.

(ii) Normalization to the sample absorption.

(iii) Subtraction of the empty cell, pure solvent and parasitic scattering.

In a general experiment where the sample is dispersed in a solvent and confined in a container, the ED-SAXS scattering intensity observed at the detector can be written as

$$\begin{aligned} I_{\rm sam}^{\rm obs}(E,\theta) = K[&I_0(E)A_{\rm tot}(E,\theta)I_{\rm sam}(E,\theta) \\ &+ I_0(E)A_{\rm tot}(E,\theta)I_{\rm solv}(E,\theta)c_{\rm solv} \\ &+ I_0(E)A_{\rm tot}(E,\theta)I_{\rm cell}(E,\theta)] \\ &+ K'[I_0(E)A_{\rm tot}(E,\theta)\Pi_{\rm s}(E,\theta)], \end{aligned} \qquad (10)$$

where $I_{\rm sam}(E,\theta)$ is the contribution from the sample molecules/particles; $I_{\rm solv}(E,\theta)$ is the contribution from the pure solvent of volume fraction $c_{\rm solv}$; $I_{\rm cell}(E,\theta)$ is the contribution from the cell containing the sample; $\Pi_{\rm s}(E,\theta)$ is the contribution from the parasitic scattering due to the collimation system and the air scattering; $A_{\rm tot}(E,\theta) = A_{\rm sam}(E,\theta)A_{\rm solv}(E,\theta)A_{\rm cell}(E,\theta)$ is the total absorption of the incident X-ray beam by the sample, $A_{\rm sam}(E,\theta)$ being the absorption of the sample only, $A_{\rm solv}(E,\theta)$ the absorption of the pure solvent and $A_{\rm cell}(E,\theta)$ the absorption of the cell windows. The absorption is defined as

$$A(E,\theta) = \frac{I_{\rm tr}(E,\theta)}{I_0(E)} = \exp\left[-\frac{\mu(E)}{\rho}\rho t\sec\theta\right]$$

where $I_{\rm tr}$ is the transmitted intensity through the sample, t is the sample thickness and $\mu(E)/\rho$ is the mass attenuation coefficient. At small angles the term $\sec\theta$ can be taken as equal to 1.

In the same way, the ED-SAXS intensities observed for the pure solvent and for the empty cell are

$$\begin{aligned} I_{\rm sam}^{\rm obs}(E,\theta) = K[&I_0(E)A_{\rm solv+cell}(E,\theta)I_{\rm solv}(E,\theta) \\ &+ I_0(E)A_{\rm solv+cell}(E,\theta)I_{\rm cell}(E,\theta)] \\ &+ K'[I_0(E)A_{\rm solv+cell}(E,\theta)\Pi_{\rm s}(E,\theta)] \end{aligned} \qquad (11a)$$

and

$$\begin{aligned} I_{\rm sam}^{\rm obs}(E,\theta) = K[&I_0(E)A_{\rm cell}(E,\theta)I_{\rm cell}(E,\theta)] \\ &+ K'[I_0(E)A_{\rm cell}(E,\theta)\Pi_{\rm s}(E,\theta)], \end{aligned} \qquad (11b)$$

where $A_{\rm solv+cell}(E,\theta) = A_{\rm solv}(E,\theta)A_{\rm cell}(E,\theta)$ is the absorption of the pure solvent in the cell.

The ED-SAXS sample intensity corrected for the empty cell scattering and for all the background scattering contributions can be obtained after measuring the quantities $I_{\rm sam}^{\rm obs}(E,\theta)$, $I_{\rm solv}^{\rm obs}(E,\theta)$, $I_{\rm cell}^{\rm obs}(E,\theta)$, $A_{\rm tot}(E,\theta)$, $A_{\rm solv+cell}(E,\theta)$, $A_{\rm cell}(E,\theta)$ and $I_0(E)$ as

$$\begin{aligned} I_{\rm sam}(E,\theta) = \Bigg[&I_{\rm sam}^{\rm obs}(E,\theta) - \frac{A_{\rm tot}(E,\theta)}{A_{\rm solv+cell}(E,\theta)} I_{\rm solv}^{\rm obs}(E,\theta)c_{\rm solv} \\ &- (1-c_{\rm solv})\frac{A_{\rm tot}(E,\theta)}{A_{\rm solv+cell}(E,\theta)} I_{\rm cell}^{\rm obs}(E,\theta)\Bigg] \\ &\times \left[A_{\rm tot}(E,\theta)I_0(E)\right]^{-1}, \end{aligned} \qquad (12)$$

where the parasitic contribution vanishes.

For very dilute solutions ($c_{\rm solv} \simeq 1$), like in many protein solution scattering experiments, the scattering from the cell vanishes when the data are corrected for the pure solvent contribution. Under the further assumption that $A_{\rm tot}(E,\theta) \simeq A_{\rm solv+cell}(E,\theta)$, the sample intensity can be obtained as

$$I_{\rm sam}(E,\theta) \simeq \frac{I_{\rm sam}^{\rm obs}(E,\theta) - I_{\rm solv}^{\rm obs}(E,\theta)}{A_{\rm tot}(E,\theta)I_0(E)}. \qquad (13)$$

The contribution of the pure solvent is not present in the case of solid samples and only normalization to the incident white-beam spectral profile and correction for the energy-dependent sample absorption have to be carried out. To do this, the transmission of the sample and the white-beam spectral profile are measured at $\theta = 0$ according to the experimental procedure reported in §3. For solid samples, the parasitic scattering can be eliminated by subtraction of the air-scattering contribution from $I_{\rm sam}^{\rm obs}(E,\theta)$. Alternatively, it can be theoretically calculated and subtracted from $I_{\rm sam}^{\rm obs}(E,\theta)$. The calculation of the parasitic intensity is lengthy and not always possible. A calculation of the parasitic intensity in our energy-dispersive case is

discussed in Appendix A and leads to the result $\Pi_s(E,\theta) \simeq \cos t/q^2$. This instrumental function can be subtracted from the experimental data after suitable scaling, so that the corrected ED-SAXS intensity is obtained. For samples with high SAXS intensity, the parasitic contribution is negligible, like for the systems studied in §4.1.

According to equation (12), the energy-dependent profiles of the white and transmitted beams have to be measured in order to extract the corrected ED-SAXS sample intensity. Unfortunately, due to detector saturation problems, these two quantities cannot be measured under the same experimental conditions as for the sample scattering intensity measurement. Realistic $A_{\rm tot}(E,\theta)$ and $I_0(E)$ profiles can be measured as described in §3 and used to normalize ED-SAXS data. Some deviations from the real profiles are, however, present, especially in the tail regions, and can become critical when smooth diffuse patterns are to be measured. In this paper, an alternative approach to correct the solution scattering data has been adopted. For a two-component system composed of large particles (*e.g.* macromolecules) and small solvent molecules, the density fluctuations of the solvent can be ignored in the relevant q range (0.01–0.3 Å^{-1}), and the solvent signal can be considered as a homogeneous background (Cotton, 1991). According to theoretical results derived from classical fluctuation theory, the solvent contributes to the background intensity as a flat profile the value of which at low q approaches:

$$I(q \rightarrow 0) = \left(\sum_i c_i f_i\right)^2 \rho_0 k_{\rm B} T \chi_T, \qquad (14)$$

where f_i and c_i are the scattering factors and the atomic fractions of all the atoms of the solvent, respectively; ρ_0 is the atomic number density, $k_{\rm B}$ is the Boltzmann constant, T is the absolute temperature and χ_T is the isothermal compressibility (Guinier & Fournet, 1955). At each angle, the measured background intensity can be regarded as a direct measure of the total instrumental function, necessary to normalize the measured sample intensity.

In conclusion, for the treatment of the solution scattering data presented in this paper, we used the following procedure: the background alone and the sample plus background scattering profiles are collected at each angle with the same instrumental setup (same slit apertures). The measured intensities are reported in terms of counts per second and per channel and the sample plus background (solvent) intensity is weighted with a factor $[A_{\rm solv+cell}(E,\theta)/A_{\rm tot}(E,\theta)]$ to correct for the different transmissions of sample and solvent. At each scattering angle, the background is subtracted from the raw data and the result is divided by the background scattering intensity. Thus, in a solution scattering experiment, the ED-SAXS intensity corrected for the overall instrumental function can be written as

$$I_{\rm sam}(E,\theta) = \frac{I^{\rm obs}_{\rm sam}(E,\theta)(A_{\rm solv+cell}/A_{\rm tot}) - I^{\rm obs}_{\rm solv}(E,\theta)}{I^{\rm obs}_{\rm solv}(E,\theta)}. \qquad (15)$$

The sample absorption can be taken into account using Victoreen's law (Victoren, 1949). Generally, the absorption process is significant at low energies and can be approximated by the function $A_{\rm coh}(E) = cE^{-3} + dE^{-4}$, where c and d are two constants and E is the X-ray energy. The absorption effect can be observed in §4.2.1, curve (*a*) of Fig. 7 for a lysozyme solution in the low-energy portions of each data set. Using the Victoreen's law correction, this effect was eliminated, as shown by curve (*b*) in the same figure. The blank scattering normalization method indicated in equation (15) does not require independent measurements of the white and the transmitted beam.

Furthermore, other corrections should be applied to account for detector effects. The correction for the escape peaks can be neglected in the present experiments and the efficiency of the solid-state Ge detector (Ge SSD) can be considered to be 100% under our experimental conditions. The correction for the finite energy resolution should be considered as well.

Besides the effect of the angular spread, in the ED technique another contribution results in the decrease of the resolution of the SAXS pattern (like any pattern collected using a Ge SSD). This contribution is due to the convolution of the SAXS pattern with the instrumental energy-transfer function $R(E)$. Such a function can be estimated by measuring the broadening of a set of fluorescence lines at different energies. From the practical point of view, fluorescence lines can be regarded as Dirac functions, centred at the characteristic energies of the emitting atoms. Due to the finite energy resolution of the Ge SSD, fluorescence lines appear as Gaussian peaks, the variance of which is an increasing function of energy. Therefore, by measuring the full width at half-maximum (FWHM) of the fluorescence peaks, $R(E)$ can be estimated. For this purpose, the fluorescence peaks of different metals (Cd, Se, Cr, Cu, Ba) were used for calibration in an energy range between 5 and 35 keV. The peaks observed were fitted using Gaussian functions and the energy dependence of the variance was found to be linear (inset in Fig. 1).

The calculated $R(E)$ is

$$R(E) = \frac{1}{\sigma(E_0)(2\pi)^{1/2}} \exp\left[-\frac{(E-E_0)^2}{2\sigma^2(E_0)}\right], \qquad (16)$$

with $\sigma^2(E_0) = 0.0064 + 0.002E_0$.

In order to obtain the actual ED-SAXS patterns, the measured intensity $I_{\rm obs}(E,\theta)$ has to be deconvoluted. However, since the FWHM of $R(E)$ appears to be negligible in comparison with the collected SAXS peaks, this correction is not essential. To substantiate this, the effect of the energy finite resolution of the detector on the theoretical Porod function ($\propto E^{-4}$) was determined and is reported in Fig. 2. The normalized ED-SAXS data collected at $\theta = 0.15^\circ$ for a TiO_2 powder sample with perfect Porodian behaviour are also reported for comparison.

The convolution of the Porod curve with $R(E)$ affects significantly the curve profile, as shown in the plot $\log[I(E)]$ *versus* $\log(E)$, where the slope changes from -4 to -3.7.

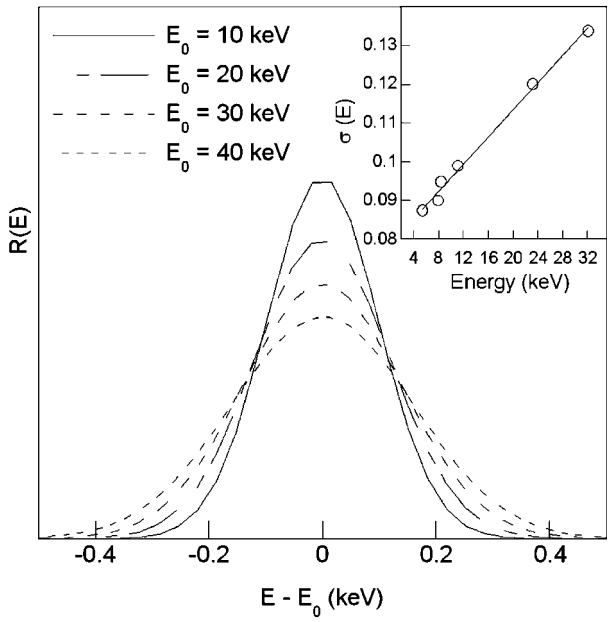

Figure 1
Effect of the energy resolution $R(E)$ on theoretical Dirac functions centred at different energies. The resulting peaks are Gaussian curves, the variances of which are energy dependent, as shown in the inset.

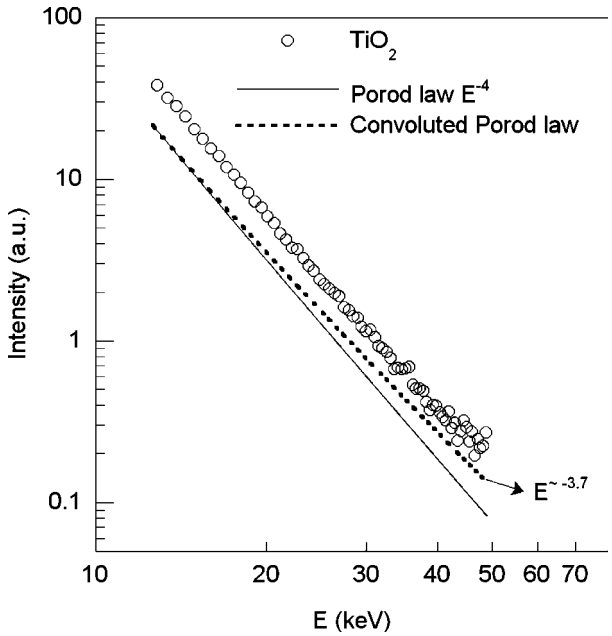

Figure 2
Effect of the energy resolution function $R(E)$ of the SSD detector on the theoretical Porod law pattern. The Porod exponent decreases slightly as the energy of the scattered photons increases owing to $R(E)$. The circles represent the experimental ED-SAXS data reported in §4.1 for a TiO_2 powder sample with perfect Porodian behaviour. The scattering angle is $\theta = 0.15°$.

However, this high-energy portion of experimental data was not used: lower energy data acquired at the subsequent scattering angle were used instead. As a consequence, one may state that the correction for $R(E)$ would result only in a reduction of the number of scattering angles. In other words, the deconvolution can be avoided, the only drawback being an increase of the number of patterns to be collected to cover the q range of interest.

3. Experimental apparatus

The apparatus used for the ED-SAXS experiments was built at the X-ray powder diffraction laboratory of the Chemistry Department in Rome. It has also been used for wide-angle X-ray scattering (WAXS) (Caminiti & Rossi Albertini, 1999) and ED diffraction experiments at intermediate angles on lipid systems (Caminiti *et al.*, 2005). A detailed description is given in previous papers (Caminiti *et al.*, 1991, 1996). As compared with usual SAXS stations, our device has a slit collimation system similar to that of a Beeman station (Ritland *et al.*, 1950). A tungsten anode tube is used as a polychromatic X-ray source and the energy of the scattered photons is detected by the Ge SSD mentioned above. The collimation system schematically depicted in Fig. 3 is composed of four slits (from F1 to F4).

Each slit is made of two independent couples of perpendicular knife-edge windows. The aperture of each slit can be adjusted for every scattering angle in order to maximize the incident beam flux at the desired angular resolution. The first slit is placed immediately after the X-ray tube, selecting a portion of the beam coming from the source and cutting the parasitic scattering from the Be window and the internal reflections in the tube. The second slit defines the angular divergence of the primary beam and its transversal section. In SAXS studies, the scattered intensity must be measured as close as possible to the scattered beam centre. As a consequence, the beam size should be the smallest possible in order to have the minimum relative uncertainty on the angle ($\Delta\theta/\theta$). In contrast, an adequate photon flux on the sample and a sufficiently large beam are necessary to reduce the acquisition time. For our measurements the vertical aperture of the slit F2 (beam-limiting slit) ranged from 0.02 to 0.2 mm. When the incident X-rays impinge on the F2 edges, parasitic scattering is generated. This is usually is removed by the insertion of a third slit after F2. The third slit plays a key role and is commonly referred to as 'guard slit'. In our apparatus this role is played by F3, placed just behind the sample. The vertical optimum aperture of F3 was chosen to be slightly larger than the vertical size of F2. In this way, parasitic scattering coming from

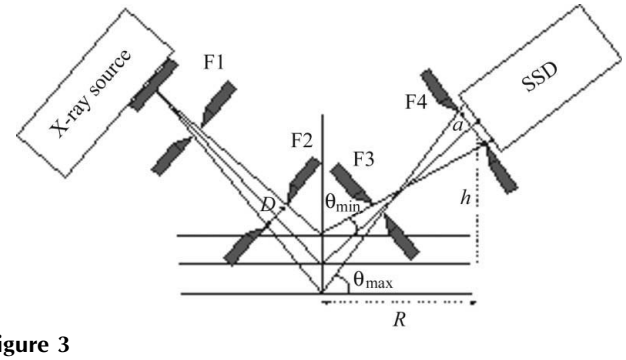

Figure 3
Schematic view of the X-ray apparatus showing the arrangement of the four collimation slits.

F2 and background scattering from the sample environment (air and sample holder) are drastically reduced. The F4 slit was placed just in front of the sensitive window of Ge SSD and its dimensions were set equal to those of F2. The horizontal aperture of all slits was 4 mm. The distance between adjacent slits was 80 mm (160 mm between F2 and F3) and the sample was placed halfway between F2 and F3. According to equation (1) and using a radiation source with an energy spectrum covering the interval $[E_1, E_2]$, the accessible q range at a given angle is $q_2 - q_1 = \alpha(E_2 - E_1)\sin\theta$. In order to obtain ED-SAXS data over a wide q range, several measurements performed at as many scattering angles are needed. The total ED-SAXS profiles were obtained by superimposing the various branches of the intensity curve after opportune corrections. Four scattering angles between 0.04 and 0.8° were selected for the measurements. The maximum observable distance is about 500 Å at the lowest scattering angle. According to equation (5), both the white beam and the transmission profiles, which depend on the energy, have to be measured to correct the raw ED-SAXS data. Usually these two measurements are challenging, since the Ge detector can be easily saturated. To solve this problem we measured the white and the transmitted beam at $\theta = 0°$ using smaller slit dimensions. Typically, the dimensions of F1 and F4 were 0.1 × 0.1 mm, while F2 and F3 were left completely opened. With these slit apertures the profiles are not significantly modified, as shown later in §4.1. The blank scattering normalization indicated in equation (15) does not require independent measurements of the white and the transmitted beam, since the sample absorption can be taken into account using Victoreen's law. Generally, the absorption process can be approximated by the expression $A_{\rm coh}(E) = cE^{-3} + dE^{-4}$, where c and d are two constants and E is the X-ray energy. The absorption effect can be observed in curve (*a*) of Fig. 7 for a lysozyme solution in the low-energy portions of each data set. Using the Victoreen's law correction, this effect was eliminated, as shown by curve (*b*) in the same figure.

4. Results and discussion

As standard samples for testing and showing the potential applications of our ED-SAXS device, we have chosen a variety of systems classically studied *via* SAXS. In this section we present the relevant ED-SAXS results and compare them with those obtained by means of a classical Kratky SAXS camera.

4.1. Metal oxides

Metal oxides and especially porous metal oxides are a very important class of materials because of their high surface area/volume ratio, which makes them very appealing in surface-related applications like catalytic processes. In addition, when mechanical properties are of concern, porosity is the dominant factor affecting the performance of bulk materials. For example, failure of structural ceramics often results from flaws originating from voids present in green compacts. Surface area is the key parameter used to characterize porosity. Specific surface area is usually determined by the Brunauer–Emmett–Teller (BET) nitrogen-absorption method which probes the 'open' pores accessible to nitrogen only. However, sometimes total porosity is the parameter of main interest. In this case SAXS can be used to carry out total surface area (total porosity) measurements since scattering arises from interfaces (inhomogeneities), regardless of the connectivity of the pores. The specific surface area, $S_{\rm sp}$, is derived from SAXS data using Porod's theory (Glatter & Kratky, 1982), the mean pore sizes and solid chords being related to $S_{\rm sp}$. From Porod's theory, the absolute value of the scattering intensity in the tail region of the SAXS curve for a generically non-particulate two-phase system with a sharp interface between the two phases depends only on the total surface of the sample S:

$$I_{\rm p}(q) = \lim_{q\to\infty} I(q) = \frac{K_{\rm p}}{q^4} \simeq I_{\rm e}(q)\frac{2\pi\Delta\rho^2 S}{q^4} \qquad (17)$$

where $K_{\rm p}$ is the so-called Porod constant, $I_{\rm e}(q)$ is the intensity scattered by a single electron, $\Delta\rho$ is the electron density variation between the solid and the porous phase. This method is very simple, but requires the calibration of the measured intensity on an absolute scale. The intrinsic difficulty of this operation for energy-dispersive measurements is evident. In order to avoid the physical damage (saturation) of the detector, the measurement of the energy-dependent transmission cannot be performed under the same geometric conditions as for the scattering measurement. Moving away from the scattering geometry entails a significant change in the spectral composition and spatial distribution of the incoming intensity, thus losing the actually required information for proper calibration. The correction for the different absorption paths of the photons (impinging on the sample at different energies) would make the calculation of the absolute intensity a formidable challenge at the present state of knowledge in this area. Only Monte Carlo model simulations would help finding reliable values for the transmission. Primarily for these reasons no ED-SAXS absolute intensity data are available in the literature, as far as we are aware. Moreover, the knowledge of the absolute intensity is not required for the derivation of the physical quantities presented in this work.

The use of absolute intensity for calculating the specific surface can be avoided by using the so-called Porod invariant:

$$Q = \int_0^\infty q^2 I(q)\,{\rm d}q = 2\pi^2 I_{\rm e}(q)\Delta\rho^2 V\varphi_{\rm s}(1-\varphi_{\rm s}), \qquad (18)$$

where $\varphi_{\rm s}$ is the volume fraction of the specimen occupied by matter. Referring to the normalization relation, the specific surface, $S_{\rm sp} = S/V$, can be calculated from the experimental intensity in arbitrary units as

$$S_{\rm sp} = \frac{\lim_{q\to\infty}[q^4 I(q)]}{V 2\pi\Delta\rho^2 I_{\rm e}(q)} = \pi\varphi_{\rm s}(1-\varphi_{\rm s})\frac{K_{\rm p}}{Q}. \qquad (19)$$

Equations (17), (18) and (19) are valid when the intensity is recorded using a pinhole collimation setup. When the scat-

tering experiment is carried out using a slit system, like a Kratky camera, the same method still applies, but slightly different equations, derived for such a kind of geometry, have to be introduced (Porod, 1951). In Fig. 4 the standard way to normalize the energy-dispersive raw data (recorded at a scattering angle $\theta = 0.8^\circ$) for a sample of titania anatase (BET standard titania from FLUKA) powder (TiO_2) is reported. The normalized and absorption-corrected ED-SAXS curves, comparable with the angular-dispersive data, are obtained from the ratio between experimental scattering data and transmitted intensity, according to equation (13).

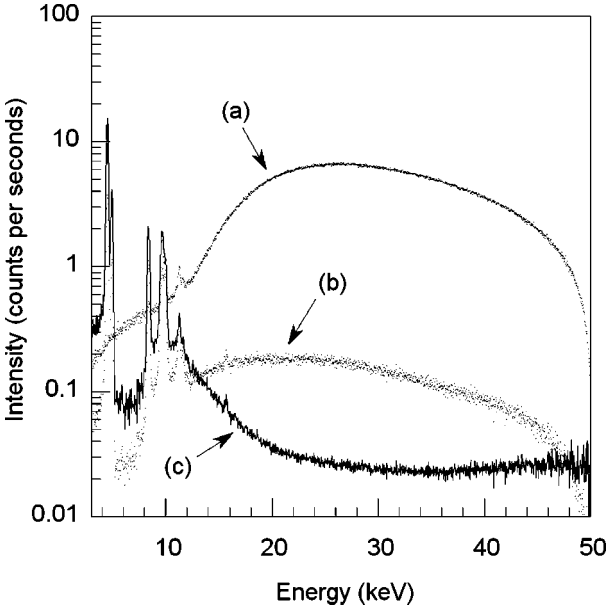

Figure 4
Comparison of the transmitted intensity ($\theta = 0^\circ$) [curve (*a*)] and the intensity scattered from the titania powder sample ($\theta = 0.8^\circ$) [curve (*b*)]. The actual scattering profile for the titania powder is curve (*c*).

The portion of the spectra below 12 keV exhibits the fluorescence lines generated by the tungsten anode and the titanium atoms. This portion was not taken into account for reconstructing the overall true small-angle intensity from the sample. The total ED-SAXS curve for titania was obtained connecting four branches of the curve collected at $\theta = 0.05$, 0.15, 0.4 and 0.8°. In Fig. 5 this curve is compared with the data obtained for the same sample by means of the classical Kratky camera. Titania does not show any correlation peak in the explored q range since the characteristic particle dimensions are greater than 600 Å (up to 1 µm from the BET analysis). As shown in Fig. 5, the Kratky SAXS profile decays following a power law q^{-3} rather than q^{-4}, as depicted by equation (17). This is due to the smearing effect of the beam cross section in the Kratky collimation system (accurately described by Guinier & Fournet, 1955). Several correction procedures have been proposed (Semenyuk & Svergun, 1991; Lake, 1967); however, the ED-SAXS data can be fitted by a power law q^{-4}, as theoretically predicted by Porod. This means that, despite the fact that the collimation system is composed of a set of rectangular slits, the acquired intensity profiles resemble those observed when a pinhole is used. In other words, the ED-SAXS spectrum is not affected by finite beam size effects.

The flat part of the curves at higher q values arises from wide-angle background. In Fig. 6 are reported both AD- and ED-SAXS profiles for a porous Al_2O_3 (alumina) sample, another very important inorganic system frequently studied at small angles. In this case, the curves show the typical diffraction pattern from porous media.

Unlike TiO_2, Al_2O_3 shows a weak correlation peak in the small-angle region. This signal is usually related to the exis-

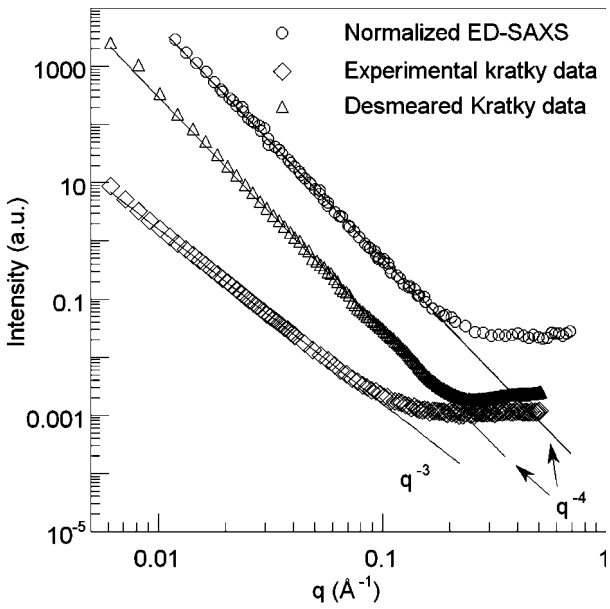

Figure 5
Porod behaviour of titania powder from AD-SAXS and ED-SAXS. Both the ED-SAXS (circles) and the desmeared AD-SAXS (squares) curves decay according to q^{-4}.

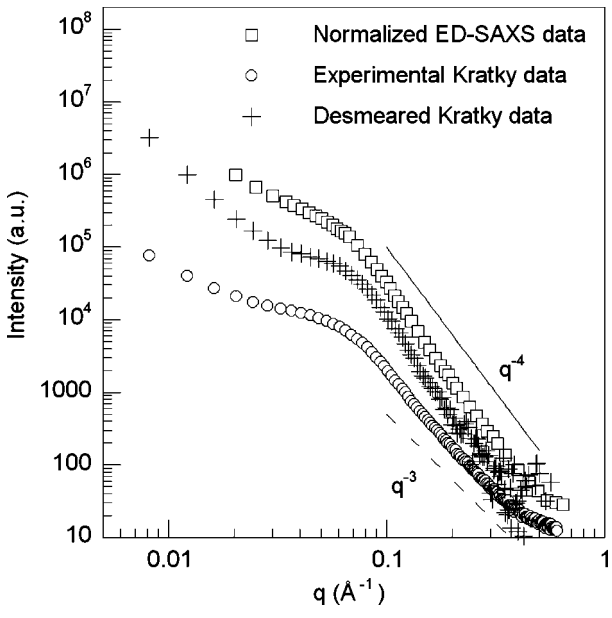

Figure 6
SAXS profiles from a porous alumina system: the squares are corrected energy-dispersive data, the crosses are desmeared Kratky data, and the circles are raw Kratky data.

Table 1
Comparison between structural parameters extracted from the Porod analysis of titania and alumina: ED-SAXS and Kratky data.

S_{sp} is the specific surface as calculated from equation (19); φ_s is the volume fraction occupied by the solid part of the sample and calculated from the ratio between the experimental bulk and the theoretical skeletal density of the sample; φ_s is equal to 0.196 and 0.75 for TiO_2 and Al_2O_3, respectively. Mean pore and solid particle diameter values were calculated from the relations $d = 4/S_{sp}$, $d_s = d\varphi_s$, $d_p = d(1 - \varphi_s)$. Data in brackets were obtained without intensity extrapolation to $q = 0$ Å^{-1}.

	AD-SAXS (Kratky)	ED-SAXS
TiO_2		
S_{sp} (m^2 cm^{-3})	25	26
Al_2O_3		
S_{sp} (m^2 cm^{-3})	169 (186)	171 (193)
φ_p	0.25	
d_p (Å)	59 (54)	58 (52)
d_s (Å)	177 (161)	175 (155)

tence of a spatial correlation between scattering domains (particles/pores), namely a well defined average inter-pore distance. The structural parameters were extracted from the analysis of both the AD- and the ED-SAXS spectra slopes and using the Porod theory [see equation (19)]. The data are summarized in Table 1. The volume fractions of the solid samples were calculated from the ratio between the experimentally determined bulk density and the theoretical skeletal density of the samples and are reported in the caption of Table 1.

As one can see, all the parameters derived from the two techniques are in good agreement. Furthermore, the quality of the data for porous alumina is good, as confirmed by what was declared by the producer datasheet (d_p = 58 Å and S_{sp} = 155 m^2 cm^{-3}, as from BET). An important consideration which can be pointed out by comparing the ED-SAXS and the AD-SAXS curves is that, in the low-angle region, the energy-dispersive curve presents a less marked minimum. This is probably a smudge effect due to the parasitic scattering arising form the collimation system of the experimental device.

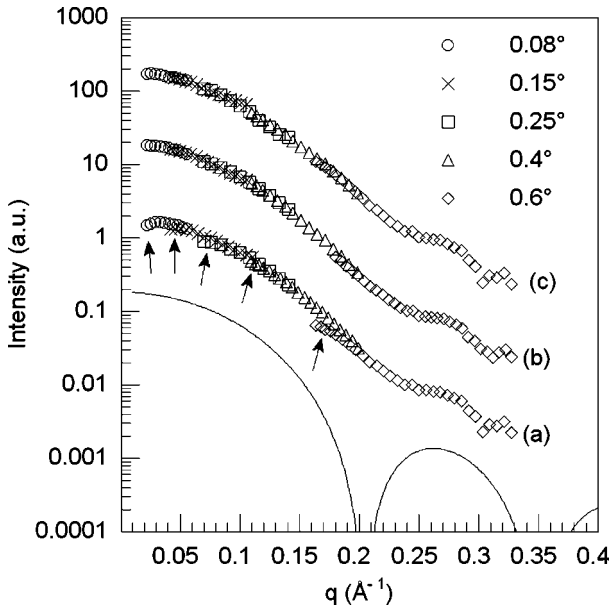

Figure 7
ED-SAXS profiles of lysozyme in water: (*a*) raw data normalized to the white spectrum profile; (*b*) same as (*a*) but after the correction for sample absorption; (*c*) data normalized using the pure solvent background scattering. The arrows are used to underline the effect of the sample absorption on every data set collected at a different scattering angle. The solid line is the theoretical scattering profile of a system of homogeneous spheres of 22 Å radius.

4.2. Biological macromolecules in solution

In this section, two ED-SAXS studies of proteins in a dilute solution are presented. In particular the shape of lysozyme molecules in a water solution was investigated *via* the characteristic function $\gamma_0(r)$ using the results of a good quality ED-SAXS experiment. The study of the size of bovine serum albumin (BSA) particles in water is also reported as a second application.

4.2.1. Lysozyme. ED-SAXS data for 2 wt% lysozyme in 0.15 *M* NaCl water solution were recorded at five different scattering angles (from 0.08 to 0.6°). The data were corrected using two normalization methods: normalization to the measured white spectrum in one case and to the background profile from pure water in the other (for details see §2). In Fig. 7 the normalized data are compared with the theoretical curve [equation (8)] calculated assuming spheres of 22 Å radius (solid line). Curve (*a*) is obtained by superimposing the data from the five scattering angles normalized to the white spectrum. At each angle the low-energy portion of this curve is affected by absorption effects (marked by arrows), which can be easily corrected *via* Victoreen's law (see §2). Curve (*b*) results from (*a*) after correction for absorption. Curve (*c*) is obtained applying the second normalization method.

For the data analysis we used the *GNOM* program (Semenyuk & Svergun, 1991). *GNOM* allows one to obtain the pair distance distribution function (PDDF) $p(r)$ from the

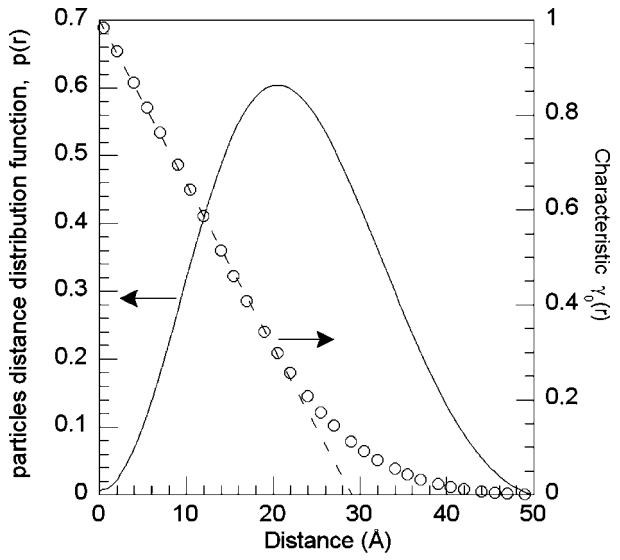

Figure 8
Pair distance distribution function $p(r)$ and characteristic function $\gamma_0(r)$ of the lysozyme water solution as obtained from the ED-SAXS curve (*c*) of Fig. 7.

normalized ED-SAXS intensity, assuming that the experimental conditions do not induce any smearing effect. In order to calculate $p(r)$, it is necessary to extrapolate the intensity to $q = 0$ Å^{-1}. This was performed according to Guinier's approximation, $I(q) = \exp(-q^2R^2/5)$. Once $p(r)$ is determined, the characteristic function $\gamma_0(r)$ can be calculated as $\gamma_0(r) = p(r)/4\pi r^2$. In Fig. 8, $p(r)$ and $\gamma_0(r)$ are reported as obtained from *GNOM* by processing the curve (*c*) of Fig. 7. From the maximum of $p(r)$ the radius of the lysozyme particles can be obtained and from the functional form of $\gamma_0(r)$ it is possible to conclude that the protein in solution has a globular shape. These results are in good agreement with those reported by Glatter *et al.* from their AD-SAXS analysis (Orthaber *et al.*, 2000).

4.2.2. Bovine serum albumin. Another ED-SAXS test was performed on bovine serum albumin (BSA), one of the most investigated proteins by small-angle techniques. In Fig. 9, the Guinier plot for four BSA water solutions at different concentrations is reported. In the inset the Guinier linear fit is illustrated for the region $R_g q < 1$, where R_g is the radius of gyration. The R_g value found for all the concentrations is about 30 Å, in good agreement with the value extrapolated at zero concentration ($R_g = 29.8$ Å) reported by Anderegg *et al.* (1955). The extrapolation of R_g at zero concentration from our experimental data appears to be a matter of speculation because of the non-negligible interparticle interference effects at concentrations greater than 5 wt%, as pointed out by Anderegg *et al.* (1955). It is important to note some behaviour problems of the ED-SAXS curves at very small q values, which are due to imprecise subtraction of the solvent contribution. For low scattering-contrast solutions like protein solutions, the air scattering is significant at small q values, thus making an accurate correction of experimental data quite difficult. These results, together with those obtained for lysozyme, demonstrate the feasibility of ED-SAXS experiments for determining size and shape of proteins in solution. A conformational study on trypsin and trypsinogen, coupling synchrotron SAXS and energy-dispersive X-ray diffraction (EDXD) measurements, has already been reported by Caracciolo *et al.* (2001).

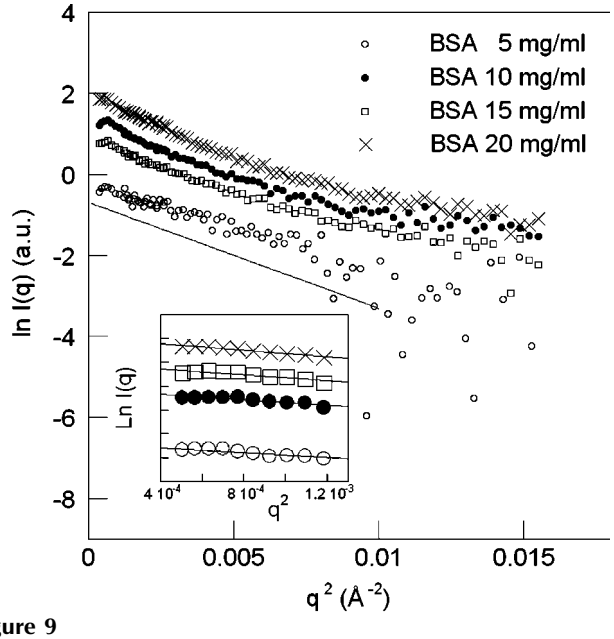

Figure 9
Guinier plots for BSA water solutions at different protein concentrations. The solid line follows the Guinier law for particles with $R_g = 30$ Å.

4.3. Size of micelles in emulsions

Aereosol sodium di-2-ethylhexylsulfosuccinate (AOT) is an anionic surfactant with two aliphatic chains which gives rise to isotropic phases in oil–water ternary systems. In such systems microemulsions form, which have recently attracted significant interest for their promising deployment as microreactors, *i.e.* for enzymatic or solid-solid reactions (Khmelnitsky *et al.*, 1989; Calandra *et al.*, 2003). The binary AOT/oil and the ternary AOT/water/oil systems are good micellar system models and have been extensively studied by light, neutron and X-ray scattering (Day *et al.*, 1979; Kotlarchyk *et al.*, 1984; Cabos & Delord, 1979). For our ED-SAXS investigations in particular, we selected the binary AOT/*n*-heptane system. The samples were contained in a sealed cell with thin Mylar windows.

In Fig. 10 SAXS profiles obtained using the above-mentioned Kratky camera are reported. The scattering patterns are the typical signatures of systems of polydisperse spherical reverse micelles at different concentrations.

ED-SAXS measurements were carried out at room temperature on the same AOT emulsions shown in Fig. 10. The raw data were normalized according to equation (15) in §2, namely by using the blank scattering from pure *n*-heptane. Scattering from the Mylar windows was also subtracted. In Fig. 11, the corrected ED-SAXS profiles for two AOT suspensions in *n*-heptane are reported.

The behaviour of both curves is clearly similar to that of the Kratky SAXS patterns shown in Fig. 10. In order to determine the size of the AOT micelles in the oil suspension, we

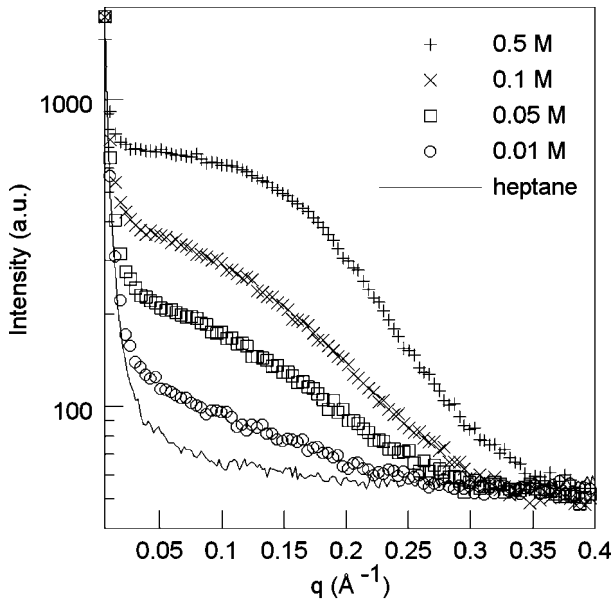

Figure 10
Smeared AOT SAXS profiles as acquired from a classical Kratky camera.

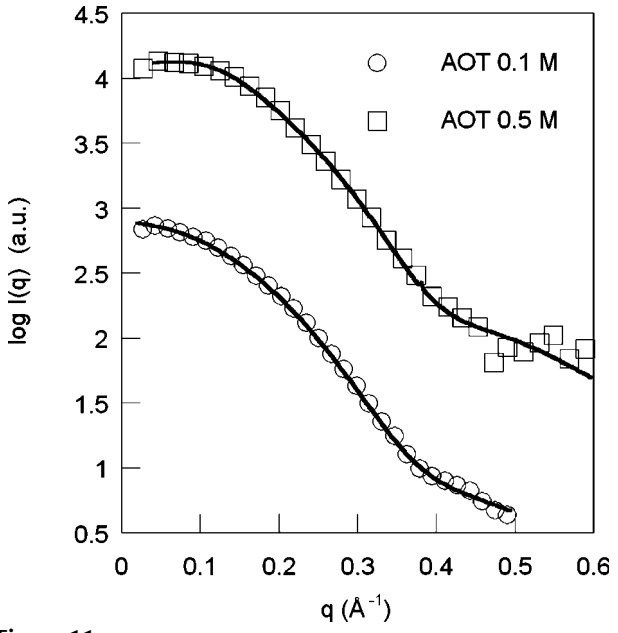

Figure 11
ED-SAXS log plot for a 0.1 and a 0.5 *M* AOT/heptane system. Solid lines are the best fits assuming a polydisperse hard-sphere model. For the higher concentration sample, the particle-to-particle interference term has been taken into account.

attempted to fit a polydisperse hard-sphere model to the data. The solid lines are the best fits obtained for the two concentrations using a Weibull radial size distribution. The resulting mean radius is 10 Å. The value of R_g and the $p(r)$ found by *GNOM* (R_g = 9 Å, *i.e.* a sphere of 11.6 Å radius) are in good agreement with those reported for binary AOT systems in the works of Kotlarchyk *et al.* (1985) and Svergun *et al.* (2000). Very much like BSA solutions, the AOT/oil ED-SAXS curves suffer from some pure solvent subtraction problems at very low q values. The deviation from the expected behaviour does not compromise an accurate determination of the sizes of the scattering objects.

4.4. Semicrystalline polymers

The possibility of obtaining correct ED-SAXS normalized intensity profiles for semicrystalline polymers has already been mentioned in a previous work (Portale *et al.*, 2004). The authors obtained a Lupolen ED-SAXS profile, which after all relevant corrections was found to be in good agreement with the profile of the same sample recorded by a classical Kratky camera. In their work, data for cold-crystallization of poly(*p*-phenylene sulfide) were presented as an example of the feasibility of time-resolved ED-SAXS experiments performed on rapidly evolving mechanisms. The agreement between angular and energy-dispersive methods was assessed by using a simple semi-quantitative approach, based on the position of the Bragg reflections from the polymeric lamellae.

Here we intend to show how to analyse the polymer morphology *via* the calculation of the correlation function $\gamma(r)$, which can be obtained by Fourier transforming a SAXS intensity profile assuming that the system is isotropic (Vonk & Kortleve, 1967):

$$\gamma(r) = \int_0^\infty I(q)q^2 \cos(2\pi rq)\,\mathrm{d}q \Big/ \int_0^\infty I(q)q^2\,\mathrm{d}q. \qquad (20)$$

A corrected ED-SAXS profile referring to a semicrystalline sample of polyhydroxybutyrate (PHB) is shown in Fig. 12. It was obtained from cold-crystallization of an amorphous glassy PHB sample at 333 K, subsequently annealed at 373 K for 1 h. The final degree of crystallinity of the sample, as determined by DSC analysis, was found to be 0.64.

In this case, the correction of raw ED-SAXS data was the same as for the inorganic solids reported in §4.1 but, in addition, the air scattering was also subtracted. As one can see, the scattering curve resembles that from a semicrystalline polymer with lamellar morphology. From the position of the scattering maximum in the Lorentzian profile $[I(q)q^2]$ the so-called long-period correlation distance L can be calculated using the Bragg law. For an ideal two-phase system, L equals the sum of the thickness of the crystalline and amorphous polymeric layers. For the investigated sample, L is about 80 Å.

In order to extract the mean thickness of crystalline and amorphous layers between two adjacent lamellae, several approaches can be followed. One of the most common is the analysis of the Fourier transform $\gamma(r)$ of the SAXS intensity, as expressed in equation (20). For the interpretation of this function the reader is referred to the work of Strobl & Schneider (1980). $\gamma(r)$ was calculated from both the ED-SAXS and AD-SAXS Kratky data acquired for the same PHB sample. Vonk's method (Vonk, 1971) was applied to extract the correlation function in both cases. Before calculating the Fourier transform, the experimental data were smoothened so

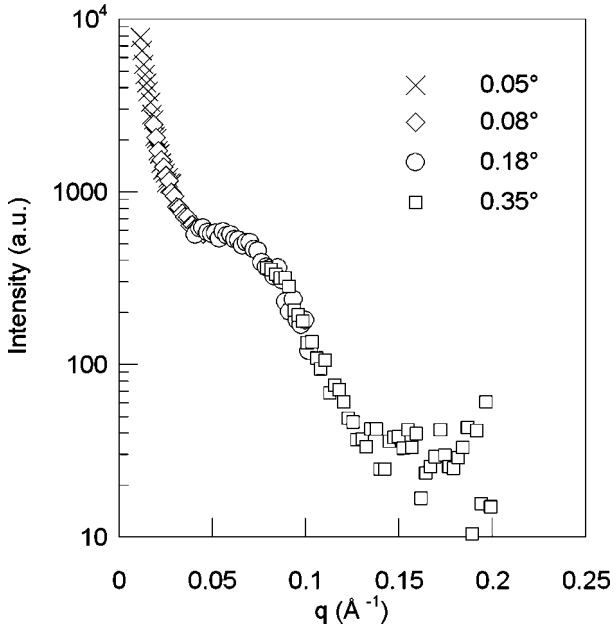

Figure 12
ED-SAXS profile referring to a semicrystalline PHB sample obtained by annealing a pre-cold-crystallized sample for 1 h at 373 K.

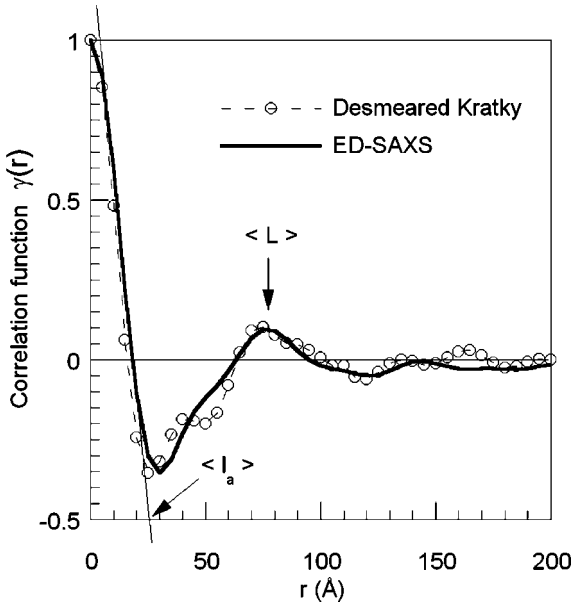

Figure 13
Comparison of the correlation functions $\gamma(r)$ obtained from the ED- and AD-SAXS data, referring to the same PHB sample.

as to obtain an acceptable correlation function and extrapolated to $q = 0$ Å^{-1}. Before the actual calculation of $\gamma(r)$, the Kratky data were desmeared using a program by Vonk (1971).

The good agreement of the two $\gamma(r)$ curves is clearly visible in Fig. 13. From the analysis of the $\gamma(r)$ profile, a mean L of 78 Å is obtained. Assuming that the sample can be modelled as an ideal two-phase system, values of 53 Å and 25 Å for the crystalline and amorphous layer thickness, respectively, are obtained. The linear crystallinity, calculated as the ratio between the crystalline thickness and L, is 0.68, which is close to the result of the DSC investigation.

5. Conclusions and future prospects

The EDXD technique has recently proven to be a powerful tool for the investigation of thermal transitions (Caminiti *et al.*, 1997, 2001; Caminiti & Rossi Albertini, 1999).

Unlike EDXD, the ED-SAXS technique is rather laborious because of the numerous corrections needed. However, some interesting considerations about the peculiar advantages of this technique induced some investigators to explore the possibility of its application to small-angle data analysis. This was the case of the earliest work of Schultz & Long (1975), which for the first time used the white radiation emitted by a conventional X-ray tube to measure the SAXS pattern from polyethylene. The appealing possibility to obtain SAXS data using the ED technique had already been reported by Bordas & Randall (1978) for measurements on biological systems using synchrotron radiation. However, we could not find any equivalent study using the laboratory ED technique in the literature. No results are available showing a detailed comparison of ED-SAXS data with other laboratory SAXS techniques. To our knowledge, the possibility of recording a complete ED-SAXS pattern over a wide q range enabling indirect Fourier transform analyses has not been demonstrated before. Starting with the idea of extending the applications of a working θ–θ ED spectrometer to SAXS measurements, the possibility of using this device in polymer morphology investigations had been proved by Portale *et al.* (2004).

In the present paper, we have explored the potential of this technique not only in polymer science, but also in view of its application to a large variety of systems classically studied by SAS. For metal oxides and polymeric materials, the standard ED data reduction can be successfully used. For solution scattering applications, especially biomacromolecules, a simple correction for the white-beam spectrum profile and sample absorption might generally fail. In this case, parasitic scattering from slits and air has to be eliminated. Using an adequate normalization for background scattering, all these undesired intensity contributions can be removed. For well known systems like lysozyme, we have shown that it is possible to obtain high-quality ED-SAXS profiles and determine the shape of the particles in solution.

In the near future, the construction of a laboratory ED X-ray machine able to conduct simultaneous WAXS/SAXS measurements will become possible. In order to carry out quantitative studies, it will be necessary to optimize all the instrumental parameters, though bearing in mind the intrinsic limitations of this technique. The deployment of vacuum pipes as well as the use of larger sample-to-detector distances could increase the angular resolution and avoid drawbacks due to incorrect air-scattering subtraction at small angular values. The reduction of the air scattering does limit the minimum attainable experimental q value, *i.e.* the maximum observable length in the samples. At present, the absolute ED-SAXS intensity calibration remains an issue on its own. It is felt that a brand new methodology should be developed from scratch, thus going well beyond the intended scope of this work.

The above limitations do not, however, change the conclusions of the present investigation.

The collection speed for any whole ED-SAXS profile presented here is slightly lower than the typical acquisition rate of a Kratky camera. It should be stressed that the data from our ED-SAXS device are not affected by smearing caused by the slit dimensions. Furthermore, owing to the geometric simplicity of the ED-SAXS experimental rig, complex sample-environment devices and chambers could be installed, such as furnaces or pressure cells, to perform *in situ* time-resolved experiments.

APPENDIX *A*
Effect of the parasitic scattering

All data were analysed without considering parasitic scattering due to collimating slits. For inorganic samples like Al_2O_3 and TiO_2, the scattered intensity is much higher than the parasitic contribution and the latter can be neglected. This term can, however, become important, especially in solution scattering experiments and has hence to be considered. In §2

we showed how the parasitic scattering can be eliminated using the blank scattering normalization method as illustrated in equation (15). We show now the effect of the parasitic scattering on the ED-SAXS curve, arising mainly from the collimation slits. Significant improvements could be achieved by enlarging the slit apertures. In Fig. 14 the log–log plot of the ED-SAXS profile is shown for one of the two AOT samples of §4.3 for each scattering angle data set. The raw intensity was corrected for the white beam profile and for the transmission effects using equation (13): a superposition of the different intensity patterns was obtained as a final result.

The change of slope below $q = 0.2$ Å^{-1} is due to the scattering from slits and follows $q^{-\alpha}$, where α is close to 1.4. Theoretically, the slit contributions to the parasitic term can be treated using the theory of X-ray diffraction from slit edges (Fresnel diffraction). In our case, the smaller the scattering angle, the narrower the slit dimensions. For $\theta = 0.08^\circ$, we have used slit dimensions of about 0.04 × 4 mm. An X-ray beam with a wavelength typically of the order of 1 Å is only slightly diffracted by a micrometre-sized slit. It was, however, shown that the diffraction of X-rays from rectangular slits can be observed using either synchrotron or sealed-tube X-ray sources and can be treated using the general equations describing the diffraction mechanism from apertures as shown *e.g.* by Le Bolloc'h *et al.* (2002), Langt *et al.* (1987) and Kellstrom (1932). By closing the slits, the sample scattered intensity decreases, while the parasitic scattering due to the slits increases. Consequently, the ratio of the sample-to-parasitic intensity can become very small at low scattering angles. For the slit-to-detector distance considered here, the X-ray diffraction should be described by the Fresnel formalism referring to a semi-infinite diffracting screen with a straight edge. An exact calculation of the diffracted intensity is generally not simple. In our case, however, $\overline{SLD} \gg D$ (with $\overline{SLD}$ denoting the slit-to-detector distance and D the slit width) and the calculations under such a condition can be simplified, since the Huygens approximation holds. For a monochromatic beam of wavelength $\lambda = hc/E$, the normalized diffracted intensity has the well known expression:

$$\frac{I(E,\theta)}{I_0(E)} = \left[\frac{\sin(\pi DE\sin\theta/hc)}{\pi DE\sin\theta/hc}\right]^2 \qquad (21)$$

where $I(E,\theta)$ is the intensity diffracted at an angle θ in the detector plane, D is the dimension of the scattering hole (slit width in our case), E is the X-ray beam energy in keV, $I_0(E)$ is the intensity of the incident X-ray beam, h is Planck's constant and c is the velocity of light. In an ED-SAXS experiment, the intensity given by equation (21) is integrated over energy intervals ΔE defined by

$$\Delta E = -Eg\theta\Delta\theta. \qquad (22)$$

In case of small symmetric slit apertures (as in the present case), the angular distribution $p(2\theta)$ is also symmetric. Using the ray-tracing method and following some simple geometrical considerations, it is possible to obtain the minimum ($\theta_{\min}$) and maximum ($\theta_{\max}$) values of θ, once the aperture D of the slit F2 is chosen (see Fig. 3). If we consider the scattering from a single slit, the angular distribution $p(2\theta)$ is a rectangular function of $\Delta\theta$ and is related to the energy distribution through

$$p(E) = (2\tan\theta/E)p(2\theta). \qquad (23)$$

The intensity scattered from the slit F2 is thereby

$$\frac{I(E,\theta)}{I_0(E)} = \frac{I(E,\theta)}{I_0(E)} = \int_{\theta_{\min}}^{\theta_{\max}} \left[\frac{\sin(\pi DE\sin\theta/hc)}{\pi DE\sin\theta/hc}\right]^2 2p(2\theta)\,\mathrm{d}\theta. \qquad (24)$$

$I(E,\theta)/I_0(E)$ can be calculated using the operational values of D, θ, $\theta_{\max}$, $\theta_{\min}$ and the experimental energy range 17–50 keV. After tedious but in principle straightforward calculations, equation (24) can be expressed in the form

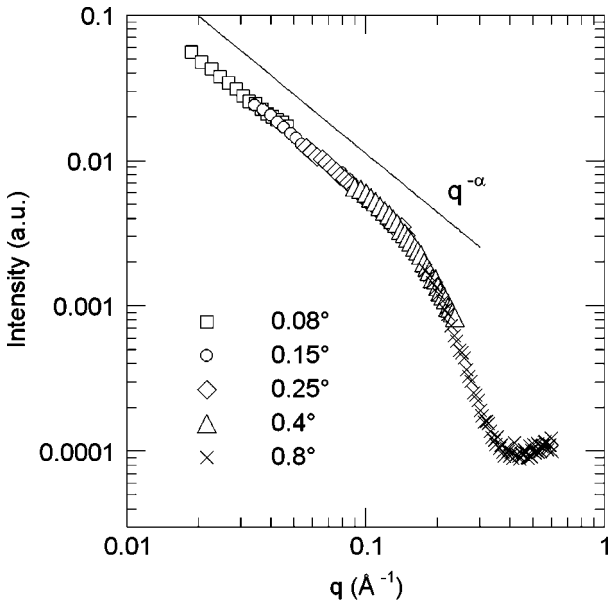

Figure 14
ED-SAXS curve for an AOT 0.5 *M* micellar suspension. The data are not corrected for the parasitic scattering contribution.

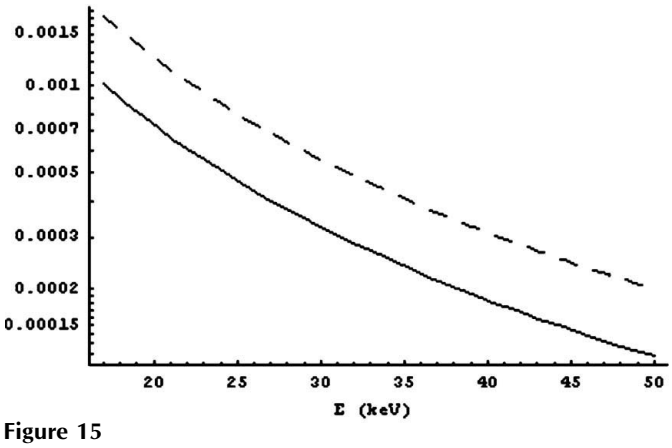

Figure 15
Diffracted intensity from F2 (solid line) calculated setting $D = 0.1$ mm, $\overline{SD} = 250$ mm, $\theta_{\min} = 4.15$ mrad and $\theta_{\max} = 4.57$ mrad. The broken line represents a function const/E^2. The intensities are on an arbitrary scale.

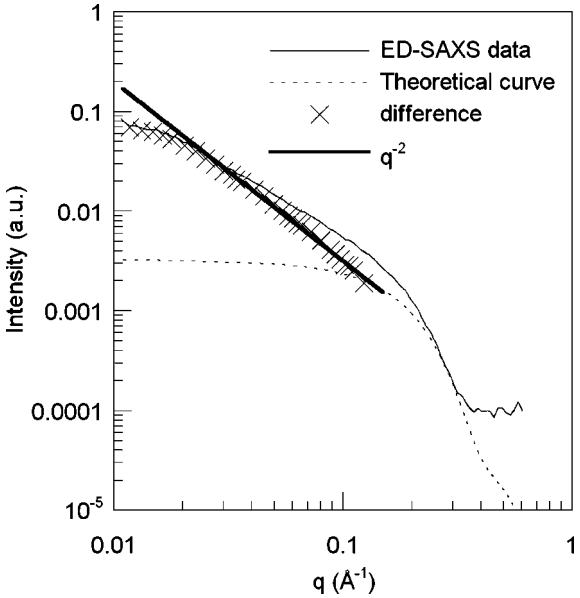

Figure 16
ED-SAXS data curve (thin solid line) for the AOT sample of §4.3 without parasitic scattering correction and theoretical curve (broken line) for a polydisperse system of spheres. The difference curve (crosses) is compared with the function const/q^2 (or const/E^2) (thick solid line) describing the parasitic scattering.

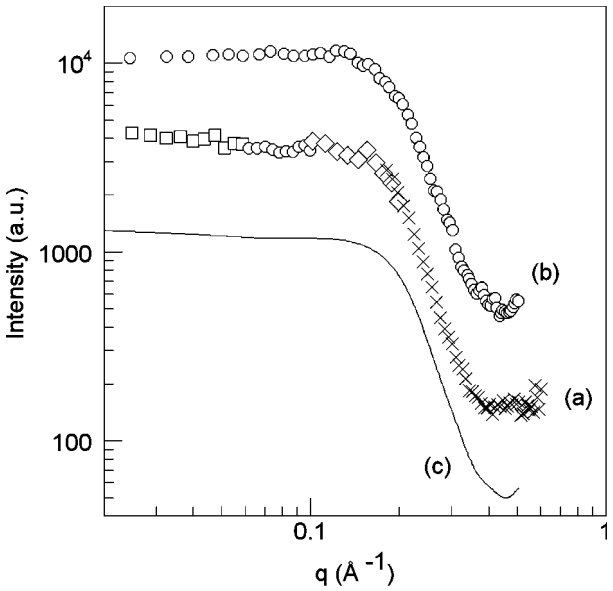

Figure 17
Scattering pattern of the AOT 0.5 *M* suspension of §4.3: (*a*) ED-SAXS profile recorded for $\overline{SD}$ = 250 mm and corrected for parasitic scattering; (*b*) ED-SAXS profile recorded using $\overline{SD}$ = 500 mm; (*c*) desmeared intensity as recorded by the Kratky camera.

$$\frac{I(E,\theta)}{I_0(E)} = \frac{1}{D^2E^2}[\text{const} + f(D, \sin\theta)] \qquad (25)$$

Fig. 15 shows the behaviour (solid line) of the intensity as given by equation (25) for a scattering angle $\theta = 0.25°$, D = 0.1 mm and $\overline{SD}$ = 250 mm, and the comparison with a function of the type const/E^2 (broken line).

The function [equation (25)] should be subtracted from the ED-SAXS data at each scattering angle. Alternatively, the unsubtracted ED-SAXS data for samples in solution can be fitted using the relevant model equations, opportunely modified to take into account the parasitic instrumental scattering. In Fig. 16, the difference between the experimental ED-SAXS curve of Fig. 14 and the theoretical curve for a polydisperse system of spheres with a mean radius of 10 Å is shown and compared with the q^{-2} trend of the parasitic scattering. In the range $0.02 < q < 0.13$ Å^{-1}, the approximation of the instrumental term with a power law q^{-2} (or E^{-2}) is satisfactory. For values of q below 0.02 Å^{-1}, negative deviations may occur, probably due to the air-scattering contribution not being taken into account.

Aiming at the confirmation of the above results, preliminary experiments were conducted using an improved configuration of the ED-SAXS apparatus. With small modifications, it has been possible to operate the apparatus at $\overline{SD}$ = 500 mm, which is twice the distance used for all the measurements reported above. In this way, larger slit dimensions can be used and the ratio between the intensity scattered from the sample and the parasitic scattering remains quite large for all the scattering angles. The results obtained with the new configuration are globally in good agreement with the data obtained from the Kratky camera and the ED-SAXS results reported above. As an example, in Fig. 17 the ED-SAXS profiles of the AOT 0.5 *M* heptane suspension are reported, obtained for $\overline{SD}$ = 250 mm after subtraction of the parasitic term [curve (*a*)] and with $\overline{SD}$ = 500 mm without any parasitic correction [curve (*b*)]. For comparison, a desmeared SAXS profile obtained using the Kratky camera for the same sample is also shown [curve (*c*)]. As can be readily seen, the agreement among the three curves is good.

We would like to thank C. Ferrero for interesting discussions on the subject and for his invaluable contribution to the final version of the manuscript.

References

Anderegg, J. W., Beeman, W. W., Shulman, S. & Kaesberg, P. (1955). *J. Am. Chem. Soc.* **77**, 2927–2937.
Bordas, J., Munro, I. H. & Glazer, A. M. (1976). *Nature (London)*, **12**, 541–545.
Bordas, J. & Randall, J. T. (1978). *J. Appl. Cryst.* **11**, 434–441.
Cabos, C. & Delord, P. (1979). *J. Appl. Cryst.* **12**, 502–510.
Calandra, P., Longo, A. & Turco Liveri, V. (2003). *J. Chem. Phys. B*, **107**, 25–30.
Caminiti, R., Caracciolo, G. & Pisani, M. (2005). *Appl. Phys. Lett.* **86**, 253902–253904.
Caminiti, R., D'Ilario, L., Martinelli, A. & Piozzi, A. (2001). *Macromol. Chem. Phys.* **202**, 2902–2914.
Caminiti, R., D'Ilario, L., Martinelli, A., Piozzi, A. & Sadun, C. (1997). *Macromolecules*, **30**, 7970–7976.
Caminiti, R. & Rossi Albertini, V. R. (1999). *Int. Rev. Phys. Chem.* **18**, 263–299.
Caminiti, R., Sadun, C., Rossi Albertini, V. R., Cilloco, F. & Felici, R. (1991). *Proceedings of the 25th National Congress of Physical Chemistry*, Cagliari, Italy, 17–21 June 1991. [Italian Patent 01261484 (1993).]

Caminiti, R., Sadun, C., Rossi Alberini, V. R., Colloco, F. & Bencivenni, L. (1996). *J. Macromol. Sci. Phys.* **835**, 199–213.
Caracciolo, G., Amiconi, G., Bencivenni, L., Boumis, G., Caminiti, R., Finocchiaro, E., Maras, B., Paolinelli, C. & Congiu Castellano, A. (2001). *Eur. Biophys. J.* **30** 163–170.
Cotton, J. P. (1991). *Introduction to Scattering Methods. In Neutron, X-ray and Light Scattering: Introduction to an Investigative Tool for Colloidal and Polymeric Systems*, edited by P. Lindner & T. Zemb, pp. 3–18. New York: Elsevier Science.
Day, R. A., Robinson, B. H., Clarke, J. H. R. & Doherty, J. V. (1979). *J. Chem. Soc. Faraday Trans. I*, **75**, 132–139.
Feigin, L. A. & Svergun, D. I. (1987). *Structure Analysis by Small-Angle X-ray and Neutron Scattering*. New York: Plenum.
Fratzl, P. (2003). *J. Appl. Cryst.* **36**, 397–404.
Glatter, O. & Kratky, O. (1982). *Small-Angle X-ray Scattering.* London: Academic Press.
Guinier, A. & Fournet, G. (1955). *Small-Angle Scattering of X-rays.* New York: Wiley.
Khmelnitsky, Y. L., Kabanov, A. V., Klyachko, N. L., Levashov, N. L. & Martinek, K. (1989). *Structure and Reactivity in Reversed Micelles*, edited by M. P. Pileni, p. 230. Elsevier: Amsterdam.
Kellstrom, G. (1932). *Nova Acta R. Soc. Sci. Upsal.* **8**, 5–65.
Kotlarchyk, M., Chen, S. H., Huang, J. S. & Kim, M. W. (1984). *Phys. Rev. A*, **29**, 2054–2069.
Kotlarchyk, M., Huang, J. S. & Chen, S. H. (1985). *J. Phys. Chem.* **89**, 4382–4386.
Lake, J. A. (1967). *Acta Cryst.* **23**, 191–194.
Langt, A. R., Kowalskit, G., Makepeacet, A. P. W., Moore, M. & Clackson, S. G. (1987). *J. Phys. D*, **20**, 541–544.
Le Bolloc'h, D., Livet, F., Bley, F., Schulli, T., Veron, M. & Metzger, T. H. (2002). *J. Synchroton Rad.* **9**, 258–265.
Orthaber, D., Bergmann, A. & Glatter, O. (2000). *J. Appl. Cryst.* **33**, 218–225.
Patterson, A. L. (1934). *Phys. Rev.* **46**, 372–376.
Porod, G. (1951). *Kolloid-Z.* **124**, 83.
Portale, G., Longo, A., D'Ilario, L., Martinelli, A. & Caminiti, R. (2004). *Appl. Phys. Lett.* **21**, 4798–4800.
Ritland, H. N., Kaesberg, P. & Beeman, W. W. (1950). *J. Appl. Phys.* **21**, 838–841.
Rossi Albertini, V. R. & Paci, B. (2002). *Rev. Sci. Instrum.* **73**, 3160–3164.
Semenyuk, A. V. & Svergun, D. I. (1991). *J. Appl. Cryst.* **24**, 537–540.
Schultz, J. M. & Long, T. C. (1975). *J. Mater. Sci.* **10**, 567–570.
Strobl, G. R. & Schneider, M. (1980). *J. Polym. Sci. Polym. Phys. Ed.* **18**, 1343–1359.
Svergun, D. I., Konarev, P. V., Volkov, V. V., Koch, M. H. J., Sager, W. F. C., Smeets J. & Blokhuis, E. M. (2000). *J. Chem. Phys.* **113**, 1651–1665.
Victoren, J. A. (1949). *J. Appl. Phys.* **20**, 1141–1147.
Vonk, C. G. (1971). *J. Appl. Cryst.* **4**, 340–342.
Vonk, C. G. & Kortleve, G. (1967). *Kolloid-Z.* **220**, 19–24.
Yu, K. L., Lee, C. H., Hwang, C. S., Tseng, H. C., Tseng, P. K., Lin, T. L., Chang, S. L., Sheu, R. J. & Chen, S. H. (1999). *Rev. Sci. Instrum.* **70**, 3233–3238.